JOINT ESTIMATION IN MRI USING HARMONIC RETRIEVAL METHODS

BY

HIEN MINH NGUYEN

B.S., Hanoi University of Technology, 2002

THESIS

Submitted in partial fulfillment of the requirements
for the degree of Master of Science in Electrical and Computer Engineering
in the Graduate College of the
University of Illinois at Urbana-Champaign, 2006

Urbana, Illinois

ABSTRACT

One of the key factors affecting functional MRI image reconstruction is field inhomogeneity. It is desirable to estimate both the distortion-free MRI image and field map simultaneously, thus compensating for image distortions caused by the field inhomogeneity. To solve this problem, which is called joint estimation problem, we propose a new non-iterative approach using harmonic retrieval (HR) methods. This connection establishes an elegant framework to solve the Joint Estimation problem through a sequence of one dimensional HR problems in which efficient solutions are available. We also derive the condition on the smoothness of the field map in order for HR techniques to recover the image with high SNR. Experimental results with the proposed method show significant improvements in MRI image reconstruction compared to methods that do not correct for field inhomogeneity.

To Father and Mother.

ACKNOWLEDGMENTS

This project would not have been possible without the support of many people. Many thanks to my adviser, Minh N. Do, who read my numerous revisions. Also thanks to Professor Bradley P. Sutton and my colleague Robert L. Morrison Jr., who offered guidance and support. And finally, thanks to my parents and my best friends who endured this long process with me, always offering support and love.

TABLE OF CONTENTS

LIST OF TABLES

LIST OF FIGURES

LIST OF ABBREVIATIONS

CRB	Cramer-Rao bound.
DFT	Discrete Fourier transform.
EPI	Echo-planar imaging.
HR	Harmonic retrieval.
IQML	Iterated quadratic maximum likelihood.
JE	Joint estimation.
LS	Least squares.
MR	Magnetic resonance.
MRI	Magnetic resonance imaging.
TLS	Total least squares.
2-D	Two-dimensional.

LIST OF SYMBOLS

a^*	Conjugate of a.
U^+	Pseudo-inverse of the matrix U.
$\overline{U}$	Matrix U omitting the first row.
$\underline{U}$	Matrix U omitting the last row.
$Diag\{a\}$	Diagonal matrix which has diagonal elements a_1, a_2, ..., a_n.
$\mathbf{k}(t)$	Sampling trajectory in k-space.
$s(\mathbf{k}(t))$	Acquired MRI data in the k-space.
$\mathbf{r}$	2-D image space.
$f(\mathbf{r})$	Continuous image.
$\omega(\mathbf{r})$	Continuous field map.
δ_1	Time delay between two consecutive MRI samples along horizontal k_x axis.
δ_2	Time delay between two consecutive MRI samples along vertical k_y axis.
Δ_1	Space distance between two consecutive MRI samples along horizontal k_x axis.
Δ_2	Space distance between two consecutive MRI samples along vertical k_y axis.
θ	Harmonics.
CRB_θ	Cramer-Rao bound on harmonics.
$\lceil x \rceil$	Rounding the real number x to the nearest larger integer.

Chapter 1

INTRODUCTION

1.1 Why Joint Estimation Problem?

Functional Magnetic Resonance Imaging (fMRI) is used to study localized brain function, both in examining healthy cognitive function and in clinical patient groups. Hence, MRI reconstruction is important for assessing the risk of brain surgery or understanding the physiological basis for neurological disorders. In the absence of magnetic field inhomogeneity MRI reconstruction is just an inverse discrete Fourier transform (DFT). However, in practice, field inhomogeneity always exists and it causes severe distortions in MRI images, such as geometric distortions and blurring effects. Thus, MRI reconstruction becomes a complicated problem and much research has been conducted on improving reconstruction performance.

To correct the distortions, standard methods involve two steps: estimating magnetic field variation and then compensating for this variation during image reconstruction [1]. However, these methods implicitly assume that the local intrinsic signal does not change its amplitude or phase during signal acquisition, which is not correct. Another approach was suggested in [2] and [3], where the idea is to combine the two steps together: reconstruct the undistorted image and field map *simultaneously* from the acquired data. This problem is called the *joint estimation* (JE) problem.

1.2 Goal of This Work

In [3] the Joint Estimation problem was solved using a nonlinear least-squares conjugate gradients (CG) method. In this work, we propose a non-iterative approach to the Joint Estimation problem using harmonic retrieval (HR) technique. We show that under certain approximation the JE problem can be treated as a sequence of 1-D HR problems in which efficient solutions are available [4]. Advantages of this approach include the running time, robustness to incorrect local minima solutions of the CG method, and no prior information for field map is needed. We concentrate on the case when k-space trajectory is *EPI (echo-planar imaging)*, which is commonly used in the practice for functional imaging. Since the Joint Estimation problem estimates both the image and field map ($2N$ unknowns), we need at least $2N$ data samples along k_y axis in k-space ($2N$ equations). Standard methods to estimate the field map also require acquiring two images in order to form this estimate [5]. We also point out a condition on the smoothness of the original field map and characterize the restoration quality as the function of field map. In the simulation part, we show experimental results that compare this approach with image reconstruction without the field map.

During real data acquisition, different issues arise, such as noise sensitivity of the collected data. Specifically, the noise causes harmonics to be closely spaced to each other. This fact can be verified from the plot of Cramer-Rao bound on the variance of the error between estimated and true harmonics versus harmonic separations. We predict the locations of wrongly recovered pixels which are caused by closely space harmonics and show the resulting image reconstruction. In the last section we present conclusions and further work.

Before we directly mathematically state the JE problem, it is useful to briefly review why image reconstruction in MRI is just an inverse DFT transform and how the presence of field inhomogeneity changes this relation. These questions are addressed in the following sections.

1.3 Image Reconstruction in MRI

Reconstruction of MR image follows next steps [6]:

1. *Signal generation:* An MR signal is generated from the *angular moments (spins)* $\boldsymbol{J}$ of object's nuclei. Since a spinning nucleus is charged, it produces a magnetic field, which is represented by *magnetic moment* $\mu = \gamma J$, where γ is a constant with units of rad/s and is known as the *gyromagnetic ratio*. In the absence of external magnetic field, all magnetic moments μ are random and the sum of these moments, which is called the *macroscopic magnetism*, is zero. To activate this macroscopic magnetism we need to line up the moments by introducing a large, homogeneous and static *main* magnetic field $\mathbf{B}_0$, which is usually applied along the vertical axis: $\mathbf{B}_0 = B_0\mathbf{k}$. $\mathbf{B}_0$ causes *nuclear precession* about $B_0\mathbf{k}$, which is described by the following equation [6]:

$$\frac{d\overrightarrow{M}}{dt} = \gamma\overrightarrow{M} \times \overrightarrow{B}_0. \tag{1.1}$$

   The angular frequency of nuclear precession is $\omega = \gamma B_0$ and is called the *Larmor frequency.*

   Next, we need to alter $\mathbf{M}$ with time. Hence, we need another magnetic field, which is called *excitation RF field* $\mathbf{B}_1$, to tip away macroscopic magnetic moment $\mathbf{M}$ from $\mathbf{k}$ direction to generate transverse component M_{xy}. The $\mathbf{B}_1$ field must be short, much smaller than main field $\mathbf{B}_0$ and must oscillate in radio frequency range. [1] In [6] $\mathbf{B}_1$ is described by the following equation:[2]

$$\mathbf{B}_1(t) = B_1^e(t)[cos(\omega_{rf}t + \varphi)\mathbf{i} - sin(\omega_{rf}t + \varphi)\mathbf{j}], \tag{1.2}$$

   The flip angle α depends on strength $B_1^e(t)$ of the magnetic field and its duration τ_p

[1] That is where the name ″RF″ comes from.

[2] Another coordinate system (i', j', k') called *rotation frame* is used, so that $\mathbf{B}_1$ field becomes stationary and pointing along i' axis [6].

[6]:

$$\alpha = \int_0^{\tau_p} \gamma \mathbf{B}_1^e(t) dt. \tag{1.3}$$

After $\mathbf{M}$ vector is flipped onto xy plane, it returns to precess about $\mathbf{B}_0$ field, not preserving its magnitude as opposed to the previous stage, where right immediately after applying $\mathbf{B}_1$ field $\mathbf{M}$ spirals down to xy plane preserving its magnitude. Two important processes occur at this stage: *longitudinal relaxation* (recovery of M_z component with time parameter T_1) and *transverse relaxation* (destruction of $\mathbf{M}_{xy}$ component with time parameter T_2). [3] This relaxation process leads to signal generation:

$$s(t) = sin(\alpha) \int_{-\infty}^{\infty} \rho(\omega) e^{-t/T_2(\omega)} e^{-i\omega t} d\omega, \tag{1.4}$$

where $\rho(\omega)$ is a spin spectral density function, $sin(\alpha)$ term shows that the signal is generated from transverse M_{xy} component and $e^{-t/T_2(\omega)}$ term shows T_2 relaxation.

2. *Signal detection in MRI*: Since RF field $\mathbf{B}_1$ is *frequency* selective, it will excite not only the spins at a specific frequency and location of that slice, but the spins from other different locations with the same frequency as well. Thus, we need to make RF field *spatially* selective. This is done using a *slice-selection gradient* $\mathbf{G}_{ss}$. [4] [6] explains how to point $\mathbf{G}_{ss}$ gradient along direction orthogonal to the chosen slice and what corresponding form of an envelope function $B_1^e(t)$ of the RF pulse will be.

3. *Image reconstruction in MRI*: After selecting a slice at a specific coordinate z_0, we need to traverse this slice to collect MRI signals and reconstruct an image of the object from these signals. To realize this stage, gradients G_x and G_y are applied. The MRI signal

[3] Here we will not discuss equations describing two relaxations. Please refer to [6] for the details. Note that T_1 and T_2 are not the times at which longitudinal and transverse relaxations are completely finished.

[4] "A linear gradient field is a magnetic field that points along the z-direction but has an amplitude varying linearly along a particular gradient direction μ_G," [6], p.143.

will conform to the following equation:

$$s(t) = \int_{-\infty}^{\infty}\int_{-\infty}^{\infty} \rho(x,y)e^{-i\gamma(B_0+G_x x+G_y y)t}dxdy, \tag{1.5}$$

where the term $e^{-i\gamma B_0 t}$ can be ignored by demodulation and relaxation term is negligible in a short time interval.

If we define new variables $k_x = \frac{\gamma}{2\pi}G_x t$ and $k_y = \frac{\gamma}{2\pi}G_y t$, [5] we will get the following equation [6]:

$$s(t) = \int_{-\infty}^{\infty}\int_{-\infty}^{\infty} \rho(x,y)e^{-2\pi(k_x x+k_y y)}dxdy. \tag{1.6}$$

This is a key principle in MRI: reconstructed image and MRI data are related by *Fourier transform*.

Since MRI data in k-space and image function are both continuous, we need to discretize them. According to Shannon sampling theorem, the k-space distance Δk between consecutive data samples $s[\mathbf{m}]$ must satisfy the following condition [6]:

$$\Delta k_x \leq \frac{1}{2k_{max}} \Rightarrow \Delta k_x \leq \frac{1}{W_x}, \tag{1.7}$$

with the same relationship applying for the other dimension, where W_x is field of view (FOV) of the object. In image domain the space distance Δx between two consecutive samples $f[\mathbf{n}]$ is defined to be $\Delta x = \frac{1}{N\Delta k_x}$. [6]. Assuming N pixels are within FOV, the minimum l_2 norm feasible reconstruction will be:

$$f[\mathbf{n}] = \Delta k_x \Delta k_y \sum_{\mathbf{n}=-\frac{N}{2}}^{\frac{N}{2}} s[\mathbf{m}]e^{-i2\pi\mathbf{n}\cdot\mathbf{m}/N}, \tag{1.8}$$

[5] Set of all values of (k_x, k_y) forms *k-space* domain.

[6] This is also called the *Fourier Pixel size* To have higher resolution, we want Δx to be small, which requires Δk to be large. Thus, in practice, we choose $\Delta k = \frac{1}{W_x}$.

which is the DFT transform. [7]

1.4 Reconstruction in the Presence of Field Inhomogeneity

In reality, the main magnetic field $\mathbf{B}_0$ is not homogeneous. According to [6], homogeneity is defined as the ratio $\frac{B_{0,max}-B_{0,min}}{B_{0,mean}}$ over some region of interest. When $\mathbf{B}_0$ is not homogeneous, the spins with the same frequency will epxerience different $\mathbf{B}_0$ field. Since Larmor frequency $\omega = \gamma B_0$, there will be some additional frequency $\Delta\omega$ due to inhomogeneity. Thus, the effective magnetic field that each spin experiences, if on-resonance condition is satisfied, is $B_1\mathbf{i}' + \frac{\Delta\omega}{\gamma}\mathbf{k}'$ [6], which causes the relation (1.8) between MRI data and image of the object to change:

$$s(t) = \int_{-\infty}^{\infty}\int_{-\infty}^{\infty} f(x,y)e^{-i\Delta\omega_0 t}e^{-2\pi(k_x x + k_y y)}dxdy. \tag{1.9}$$

In other words, the relation between MRI data and image of the object is no longer just a Fourier transform. The term $\Delta\omega_0$ is called *field map* and has units of rad/s. This term causes distortions in the reconstructed image.

[7] Note that the truncation of infinite image samples $f[n]$ leads to Gibbs artifact at discontinuities in the reconstructed image.

Chapter 2

PROPOSED APPROACH

2.1 Mathematical Model of the Problem

Given the signal during the readout $s(t)$ with specific k-space trajectory $\mathbf{k}(t)$, the JE problem recovers the image $f(\mathbf{r})$ and the field map $w(\mathbf{r})$ as described in the following continuous equation:

$$s(\mathbf{k}) = \int f(\mathbf{r}) e^{-i\omega(\mathbf{r})t} e^{-i2\pi(\mathbf{k}(t)\cdot\mathbf{r})} d\mathbf{r}. \tag{2.1}$$

Assume the object has size $N_2 \times N_1$. To discretize this problem, we assume the voxel basis $\varphi_T(\mathbf{r})$ for the continuous image and the voxel basis $\psi_T(\mathbf{r})$ for continuous field map to be 2-D square boxes (Haar bases) [7], [8] in 2D. The subscript T indicates image resolution: $T_1 = \frac{1}{N_1}$ and $T_2 = \frac{1}{N_2}$. The bases are illustrated in Fig. 2.1:

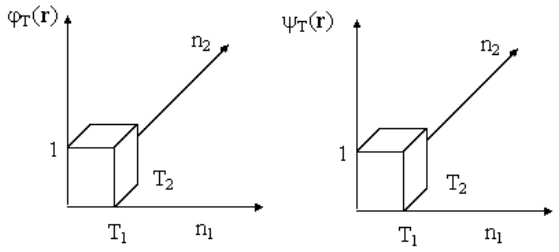

Figure 2.1: Image basis $\varphi_T(\mathbf{r})$ and field map basis $\psi_T(\mathbf{r})$.

Continuous functions $f(\mathbf{r})$ and $\omega(\mathbf{r})$ are linear combinations of these voxel bases and can be expressed as the following:

$$
\begin{aligned}
f(\mathbf{r}) &= \sum_{n_1=0}^{N_1-1}\sum_{n_2=0}^{N_2-1} f_T[\mathbf{n}]\varphi_T(\mathbf{r}-T\mathbf{n}), \qquad (2.2)\\
\omega(\mathbf{r}) &= \sum_{n_1=0}^{N_1-1}\sum_{n_2=0}^{N_2-1} \omega_T[\mathbf{n}]\psi_T(\mathbf{r}-T\mathbf{n}).
\end{aligned}
$$

Plug Eq. (2.2) into continuous Eq. (2.1) and simplify the expression using *non-overlapping* property of the defined bases:

$$
\begin{aligned}
s(\mathbf{k}) &= \int \sum_{n_1=0}^{N_1-1}\sum_{N_2=0}^{N_2-1} f_T[\mathbf{n}]\varphi_T(\mathbf{r}-T\mathbf{n}) e^{-i\sum_{l_1=0}^{N-1}\sum_{l_2=0}^{N-1}\omega_T[\mathbf{l}]\psi_T(\mathbf{r}-T\mathbf{l})\cdot t(\mathbf{k})} e^{-i2\pi\mathbf{k}\cdot\mathbf{r}} d\mathbf{r}\\
&= \sum_{n_1=0}^{N_1-1}\sum_{n_2=0}^{N_2-1} f_T[\mathbf{n}] \int \varphi_T(\mathbf{r}-T\mathbf{n}) \prod_{\mathbf{l}} \underbrace{e^{-i\omega_T[\mathbf{l}]\psi_T(\mathbf{r}-T\mathbf{l})\cdot t(\mathbf{k})}}_{\substack{e^0,\,\mathbf{n}\neq\mathbf{l}\\ e^{-i\omega_T[\mathbf{n}]\cdot 1\cdot t(\mathbf{k})},\,\mathbf{n}=\mathbf{l}}} e^{-i2\pi\mathbf{k}\cdot\mathbf{r}} d\mathbf{r}\\
&= \sum_{n_1=0}^{N_1-1}\sum_{n_2=0}^{N_2-1} f_T[\mathbf{n}] e^{-i\omega_T[\mathbf{n}]\cdot t(\mathbf{k})} \int \varphi_T(\mathbf{r}-T\mathbf{n}) e^{-i2\pi\mathbf{k}\cdot\mathbf{r}} d\mathbf{r}\\
&= \sum_{n_1=0}^{N_1-1}\sum_{n_2=0}^{N_2-1} f_T[\mathbf{n}] e^{-i\omega_T[\mathbf{n}]\cdot t(\mathbf{k})} \Phi_T(\mathbf{k}) e^{-i2\pi T\mathbf{k}\cdot\mathbf{n}}.
\end{aligned}
$$

For simplicity, from now on we will denote $s(\mathbf{k})$ by $\frac{s(\mathbf{k})}{\Phi_T(\mathbf{k})}$, so the discretized form of JE problem is

$$
s(k) = \sum_{n_1=0}^{N_1-1}\sum_{n_2=0}^{N_2-1} f_T[\mathbf{n}] e^{-i\omega_T[\mathbf{n}]\cdot t(\mathbf{k})} e^{-i2\pi T\mathbf{k}\cdot\mathbf{n}}. \qquad (2.3)
$$

Specifically, we assume an EPI trajectory $\mathbf{k}$ as described in Fig. 2.2.

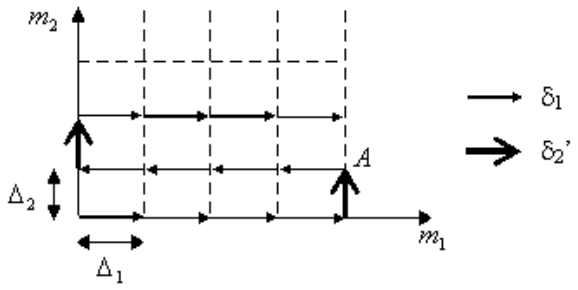

Figure 2.2: EPI sampling trajectory: Δ_1, Δ_2 are sampling intervals in k-space and $\delta_1, \delta_2^{'}$ are time delays between samples as denoted by the arrows.

2.2 Problem Analysis

We denote those k-space lines along which the data is acquired from left to the right as *forward* lines and lines along which the data is acquired from right to the left as *backward* lines.

Let δ_1, δ_2' be the time delays and Δ_1, Δ_2 be the space distances between two consecutive samples of the EPI trajectory along horizontal and vertical axes, respectively (Fig. 2.2). The total number of samples along horizontal and vertical axes is M_1 and M_2.

To convert the problem (2.3) into a 2-D problem, we express $t(\mathbf{m})$, $\mathbf{k}(\mathbf{m})$, and $\mathbf{r}(\mathbf{n})$ in the mathematical forms. From Fig. 2.2, the timing delay for forward lines is:

$$t(\mathbf{m}) = m_1\delta_1 + m_2\delta_2 \tag{2.4}$$

and the timing delay for backward lines is

$$t(\mathbf{m}) = (M_1 - 1 - m_1)\delta_1 + m_2\delta_2, \tag{2.5}$$

where δ_2 is a distance from origin along EPI trajectory until point A (see Fig 2.2). In other words,

$$\delta_2 = \delta_1(M_1 - 1) + \delta_2'.$$

The function $k(\mathbf{m})$ has one single form for both forward and backward lines. For simplicity in derivation, we assume that k-space sampling starts from the origin as it is depicted in Fig. 2.2:

$$\mathbf{k}(\mathbf{m}) = \begin{pmatrix} m_1\Delta_1 \\ m_2\Delta_2 \end{pmatrix}. \tag{2.6}$$

The function $\mathbf{r}(\mathbf{n})$ can be expressed as

$$\mathbf{r}(\mathbf{n}) = \begin{pmatrix} \frac{1}{N_1}n_1 \\ \frac{1}{N_2}n_2 \end{pmatrix}, \tag{2.7}$$

where $\mathbf{n} = (n_1, n_2)$ is a Cartesian coordinate system.

2.3 Derivation

We consider the forward case first and then show under some practical assumptions that the backward case will be exactly the same as the forward case.

1. *Forward lines*: substituting Equations (2.4), (2.6), and (2.7) into (2.3), we obtain:

$$s[m_1, m_2] = \sum_{\mathbf{n}} f[\mathbf{n}] e^{-im_1(\omega[\mathbf{n}]\delta_1 + \frac{2\pi}{N_1}\Delta_1 n_1)} e^{-im_2(\omega[\mathbf{n}]\delta_2 + \frac{2\pi}{N_2}\Delta_2 n_2)}. \tag{2.8}$$

   In practice, the time interval δ_1 between two samples along the horizontal k-space line is two orders of magnitude smaller than the time δ_2' needed for the gradient to change its value and go to the next line, therefore $\delta_1 \ll \delta_2$. Hence, we can assume that

$\omega[\mathbf{n}]\delta_1 \approx 0$. A similar approximation is widely used for EPI [1]. Setting $\Delta_1 = 1$ and taking inverse DFT both sides of equation along horizontal m_1 direction, we get:

$$\widetilde{s}[n_1, m_2] = \sum_{n_2=0}^{N_2-1} f[n_1, n_2] e^{-i(\omega[\mathbf{n}]\delta_2 + \frac{2\pi}{N_2} n_2) m_2}, \qquad (2.9)$$
$$m_2 = 0, ..., M_2 - 1.$$

Comparing with the 1D HR problem

$$s[m] = \sum_{n=0}^{N-1} a_n e^{i\phi_n m}, \qquad (2.10)$$

$$m = 0, ..., M-1 \quad \text{and} \quad M \geq 2N,$$

we see that (2.9) is a sequence of N_1 1D-HR problems where for a *fixed* n_1 we can assign $a_n = f[n_1, n_2]$ and $\phi_n = -\left(\frac{2\pi}{N_2} n_2 + \omega[\mathbf{n}]\delta_2\right)$, which can be solved when $M \geq 2N$ (M data samples, $2N$ unknowns a_n and ϕ_n). This means the number of samples collected along the vertical k-space axis should be double the reconstructed size along same axis. Different methods exist to solve the HR problem, which will be reviewed in the next section.

2. *Backward lines*: by the same token, we get the following equation for backward case:

$$s[m_1, m_2] = \sum_{\mathbf{n}} f[\mathbf{n}] e^{-i(\omega[\mathbf{n}](M_1 - 1 - m_1)\delta_1 + \omega[\mathbf{n}] m_2 \delta_2)}$$
$$e^{-i\frac{2\pi}{N_1}(m_1 n_1 \Delta_1)} e^{-i\frac{2\pi}{N_2}(m_2 n_2 \Delta_2)}. \qquad (2.11)$$

Assuming again that $w[\mathbf{n}]\delta_1 \approx 0$, we obtain the same problem formulation as equation (2.9) in forward case. As a result, with this assumption, the forward and backward lines can be treated in the same way.

In the case where k-space is symmetric, the acquired data is $s[\tilde{k_1}, \tilde{k_2}]$, where $-\frac{N_1}{2} \leq \tilde{k_1} < \frac{N_1}{2}$ and $-\frac{N_2}{2} \leq \tilde{k_2} < \frac{N_2}{2}$. Since $s[k_1, k_2]$ corresponds to the image $f[\mathbf{n}]$, the shift in k-space, $s[k_1 - \frac{N}{2}, k_2 - \frac{N}{2}]$ leads to a modulation term in the spatial domain: $\tilde{f}[\mathbf{n}] = f[\mathbf{n}]e^{-j\pi n_1}e^{-j\pi n_2}$.

2.4 Algorithm for Mapping to HR Problem

Below is the summary of proposed algorithm (see Fig. 2.3):

1. Given acquisition data, take inverse DFT along m_1 axis, call it $\widetilde{s}[n_1, m_2]$.

2. For each fixed value of n_1 solve following 1-D HR problem to recover field map $\omega[\mathbf{n}]$ and image $\tilde{f}[\mathbf{n}]$:

$$\widetilde{s}[n_1, m_2] = \sum_{n_2} f[n_1, n_2]e^{-i(\omega[\mathbf{n}] + \frac{2\pi}{N_2} n_2 \delta_2)m_2}.$$

3. Estimated image is $f[\mathbf{n}] = \frac{\tilde{f}[\mathbf{n}]}{(-1)^{n_1}(-1)^{n_2}}$.

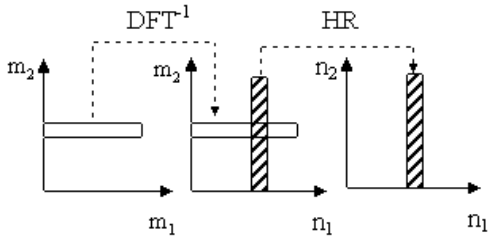

Figure 2.3: Illustration of the proposed approach.

Chapter 3

DIFFERENT METHODS FOR SOLVING HARMONIC RETRIEVAL PROBLEM

Recall HR problem described in Eq. (2.10): given M samples τ_k, we need to recover N samples a_n and N samples z_n. Different methods exist to solve HR problem, so in this part we will emphasize the key ideas of each method, rather than describing the whole algorithm.

3.1 Least Squares (LS) Prony Method

This is the oldest and most standard method for solving the HR problem [9], [10]. Consider Eq. (2.10). It follows that z_n are roots of the characteristic equation with coefficients p_i, $i = 0, ..., N$:

$$p_0 r^N + p_1 r^{N-1} + ... + p_{N-1} r + p_N = 0. \tag{3.1}$$

Hence, the data samples τ_i satisfy the following N-order difference equation:

$$p_N \tau_k + p_{N-1} \tau_{k+1} + ... + p_1 \tau_{k+N-1} + p_0 \tau_{N+k} = 0, \tag{3.2}$$

where $k = 0, 1, ..., M - N - 1$.

Dividing both sides of the difference equation by p_0, we get the following matrix equation:

$$-\begin{pmatrix} \tau_N \\ \tau_{N+1} \\ \cdots \\ \tau_{M-1} \end{pmatrix} = \begin{pmatrix} \tau_0 & \tau_1 & \cdots & \tau_{N-1} \\ \tau_1 & \tau_2 & \cdots & \tau_N \\ & \cdots & & \\ \tau_{M-N-1} & \tau_{M-N} & \cdots & \tau_{M-2} \end{pmatrix} \begin{pmatrix} \widehat{p}_N \\ \widehat{p}_{N-1} \\ \cdots \\ \widehat{p}_1 \end{pmatrix}, \tag{3.3}$$

where $\widehat{p} = p_i/p_0$. Call the matrix in the above equation T. It is a Hankel nonsingular matrix. Inverting this matrix gives coefficients $\widehat{p_i}$, and z_n can be found as roots of the polynomial with coefficients p_i. However, there exists another way to find the roots: z_n are eigenvalues of the following matrix C:

$$C = \begin{pmatrix} 0 & 0 & \cdots & 0 & -p_N \\ 1 & 0 & \cdots & 0 & -p_{N-1} \\ & & \cdots & & \\ 0 & 0 & \cdots & 1 & -p_1 \end{pmatrix}.$$

Proof:

$$z^N = -\sum_{n=1}^{N} p_n z^{N-n} \qquad \Rightarrow$$

$$\underbrace{[z \quad z^2 \quad z^3 ... \quad z^N]}_{z[1 \quad z \quad z^2 ... \quad z^{N-1}]} = [1 \quad z \quad z^2 ... \quad z^{N-1}]C.$$

Hence, z is eigenvalue of C.

3.2 Forward-Backward Method

This approach is similar to LS Prony method, but it considers a specific case when z_n are on the unit circle [9] which means that $|z| = 1$ (hence, this method is appropriate for JE problem). If z_n are roots of polynomial (3.1), so are $\frac{1}{z_n^*}$ - reciprocal complex conjugates of z_n. This means that the following difference equation must be hold also:

$$z^{-N} + p_1^* z^{-(N-1)} + p_2^* z^{-(N-2)} + ... + p_N^* = 0. \tag{3.4}$$

Thus, Eq. (3.5) can be expanded [9], [10] to give a more precise solution for $\widehat{p}_i$:

$$-\begin{pmatrix} \tau_N \\ \tau_{N+1} \\ \cdots \\ \tau_{M-1} \\ \tau_0^* \\ \cdots \\ \tau_{M-N-2}^* \end{pmatrix} = \begin{pmatrix} \tau_0 & \tau_1 & \cdots & \tau_{N-1} \\ \tau_1 & \tau_2 & \cdots & \tau_N \\ & \cdots & & \\ \tau_{M-N-1} & \tau_{M-N} & \cdots & \tau_{M-2} \\ \tau_{N-1}^* & \tau_{N-2}^* & \cdots & \tau_0^* \\ & \cdots & & \\ \tau_{M-2}^* & \tau_{M-3}^* & \cdots & \tau_{M-N-1}^* \end{pmatrix} \begin{pmatrix} \widehat{p}_N \\ \widehat{p}_{N-1} \\ \cdots \\ \widehat{p}_1 \end{pmatrix}. \tag{3.5}$$

3.3 Total Least Squares (TLS) Prony Method

This method concentrates on reducing the effect of noise [9]. In the presence of additive noise, Eq. (3.5) becomes [10]:

$$(T+E)p = (\tau + e)$$

or

$$\begin{pmatrix} T+E & | & \tau+e \end{pmatrix} \begin{pmatrix} p \\ -1 \end{pmatrix} = 0.$$

This means that vector $\begin{pmatrix} p \\ -1 \end{pmatrix} \in N(\begin{pmatrix} T+E & | & \tau+e \end{pmatrix})$, where $N(\cdot)$ stands for the null space. In other words, $dim(N\begin{pmatrix} T+E & | & \tau+e \end{pmatrix}) \geq 1$ or $rank(\begin{pmatrix} T+E & | & \tau+e \end{pmatrix}) \leq N$. Using Eckart-Yuong theorem [10] we can approximate noisy data matrix with its N^{th} order SVD approximation: $\begin{pmatrix} T+E & | & \tau+e \end{pmatrix} \approx \sum_{k=1}^{N} \sigma_k u_k v_k^H$. It then follows that desired vector $\begin{pmatrix} p \\ -1 \end{pmatrix}$ is a right singular vector corresponding to the smallest singular value of the noisy data matrix [10].

3.4 Iterated Quadratic Maximum Likelihood (IQML) Method

This method is an iterative approach to HR problem and it reduces the effect of noise of the input data. Denote B^H as the following matrix:

$$\begin{pmatrix} p_N & p_{N-1} & ... & p_0 & 0 & ... & 0 \\ 0 & p_N & ... & p_1 & p_0 & ... & 0 \\ & & & \cdots & & & \\ 0 & ... & p_N & p_{N-1} & 0 & ... & 0 \end{pmatrix}.$$

It is easy to verify that the following condition must be satisfied:

$$B^H Z = 0.$$

From above condition [10] proves that:

$$R(Z^{\perp}) = R(B). \tag{3.6}$$

This approach views HR problem as a minimization problem decoupled into two steps: minimizing **a** and minimizing **z** separately, which means that $\widehat{z} = min_z min_a ||\tau - Za||_2^2$ [10], where:

$$Z = \begin{pmatrix} z_1^0 & z_2^0 & \cdots & z_N^0 \\ z_1^1 & z_2^1 & \cdots & z_N^1 \\ & & \cdots & \\ z_1^{M-1} & z_2^{M-1} & \cdots & z_N^{M-1} \end{pmatrix}, \tag{3.7}$$

$$\tau = \begin{pmatrix} \tau_0 \\ . \\ . \\ . \\ \tau_{M-1} \end{pmatrix}, \qquad a = \begin{pmatrix} a_1 \\ . \\ . \\ . \\ a_N \end{pmatrix}.$$

It follows that the solution will be such z_n which minimize the l_2-norm of the projection of the data τ onto the subspace orthogonal to the range of the matrix Z. Using 3.6 it follows that we need to find such z_n that are solutions of the minimization problem $\widehat{z} = argmin_z ||P_{R(B)}\tau||^2 = \tau^H B(B^H B)^{-1} B^H \tau$. Thus we can determine z_n iteratively.

3.5 Pencil-Based Method

This method uses a clever expansion of the original HR equation (2.10) into diagonal matrices of a_n and z_n. Expanding the original HR problem we get

$$\begin{pmatrix} \tau_k \\ \tau_{k+1} \\ ... \\ \tau_{M-N-1+k} \end{pmatrix} = \begin{pmatrix} z_1^k & z_2^k & ... & z_N^k \\ z_1^{k+1} & z_2^{k+1} & ... & z_N^{k+1} \\ & \cdots & & \\ z_1^{M-N-1+k} & z_2^{M-N-1+k} & ... & z_N^{M-N-1+k} \end{pmatrix} \begin{pmatrix} a_1 \\ a_2 \\ ... \\ a_N \end{pmatrix}$$

$$= \begin{pmatrix} z_1^0 & z_2^0 & ... & z_N^0 \\ z_1^1 & z_2^1 & ... & z_N^1 \\ & \cdots & & \\ z_1^{M-N-1} & z_2^{M-N-1} & ... & z_N^{M-N-1} \end{pmatrix} Diag\{a\} \begin{pmatrix} z_1^k \\ z_2^k \\ ... \\ z_N^k \end{pmatrix}. \quad (3.8)$$

Then it follows that:

$$\begin{pmatrix} \tau_0 & \tau_1 & ... & \tau_{N-1} \\ \tau_1 & \tau_2 & ... & \tau_N \\ & \cdots & & \\ \tau_{M-N-1} & \tau_{M-N} & ... & \tau_M \end{pmatrix} = \begin{pmatrix} z_1^0 & z_2^0 & ... & z_N^0 \\ z_1^1 & z_2^1 & ... & z_N^1 \\ & \cdots & & \\ z_1^{M-N-1} & z_2^{M-N-1} & ... & z_N^{M-N-1} \end{pmatrix} Diag\{a\} \times$$
$$\begin{pmatrix} \tau_0 & \tau_1 & ... & \tau_{N-1} \\ \tau_1 & \tau_2 & ... & \tau_N \\ & \cdots & & \\ \tau_{M-N-1} & \tau_{M-N} & ... & \tau_M \end{pmatrix} \times$$
$$\begin{pmatrix} z_1^0 & z_1^1 & ... & z_1^{N-1} \\ z_2^0 & z_2^1 & ... & z_2^{N-1} \\ & \cdots & & \\ z_N^0 & z_N^1 & ... & z_N^{N-1} \end{pmatrix}. \tag{3.9}$$

Thus, we can show that [9]:

$$\underbrace{\begin{pmatrix} \tau_1 & \tau_2 & ... & \tau_N \\ \tau_2 & \tau_3 & ... & \tau_{N+1} \\ & \cdots & & \\ \tau_{M-N} & \tau_{M-N+1} & ... & \tau_{M+1} \end{pmatrix}}_{T\{1,N\}} = \underbrace{\begin{pmatrix} z_1^0 & z_2^0 & ... & z_N^0 \\ z_1^1 & z_2^1 & ... & z_N^1 \\ & \cdots & & \\ z_1^{M-N-1} & z_2^{M-N-1} & ... & z_N^{M-N-1} \end{pmatrix}}_{Z\{0,M-N-1\}} \times$$
$$Diag\{a\}Diag\{z\} \begin{pmatrix} z_1^0 & z_1^1 & ... & z_1^{N-1} \\ z_2^0 & z_2^1 & ... & z_2^{N-1} \\ & \cdots & & \\ z_N^0 & z_N^1 & ... & z_N^{N-1} \end{pmatrix}.$$

It follows that z_n are generalized eigenvectors of matrices $T\{0, N-1\}$ and $T\{1, N\}$.

3.6 Subspace-Based Method

This method [11] is based on a simple observation: we can decompose the original HR problem into the following matrix equation:

$$\underbrace{\begin{pmatrix} \tau_0 & \tau_1 & \dots & \tau_{N-1} \\ \tau_1 & \tau_2 & \dots & \tau_N \\ \cdot & \cdot & \cdot & \cdot \\ \tau_{M-1} & \tau_M & \dots & \tau_{M+N-2} \end{pmatrix}}_{T} = \underbrace{\begin{pmatrix} z_0^0 & z_1^0 & \dots & z_{N-1}^0 \\ z_1^1 & z_1^1 & \dots & z_{N-1}^1 \\ \cdot & \cdot & \cdot & \cdot \\ z_0^{M-1} & z_1^{M-1} & \dots & z_{N-1}^{M-1} \end{pmatrix}}_{U} Diag\{a\} \times$$

$$\underbrace{\begin{pmatrix} z_0^0 & z_0^1 & \dots & z_0^{M-1} \\ z_1^0 & z_1^1 & \dots & z_1^{M-1} \\ \cdot & \cdot & \cdot & \cdot \\ z_{N-1}^0 & z_{N-1}^1 & \dots & z_{N-1}^{M-1} \end{pmatrix}}_{V^H}. \tag{3.10}$$

Note that this factorization is not unique. Denote $\overline{U}$ is a matrix U omitting the first row and $\underline{U}$ is a matrix U omitting the last row. [1] Then, it is easy to see that $Diag\{z\} = \underline{U}^+ \cdot \overline{U}$. Noticing that matrix U is nothing but the set of left singular vectors of matrix T, we can recover z_n.

[1] Hence, the term ″shifted subspaces″ comes from.

Table 3.1: Comparison of different HR techniques.

Method	SNR of z (db)	SNR of τ (db)
LS Prony	30.26	39.09
Forward Backward	41.45	63.91
IQML	78.59	76.15
Pencil-Based	27.46	20.44
Subspace-Based	42.72	63.93
Total LS Prony	41.44	63.91

3.7 Comparison

Table 3.1 compares different HR methods in terms of SNR of recovered z_n and SNR of recovered data. In this experiment ground true a_n were complex, normally randomly generated with zero mean, variance $\sigma^2 = 1$, while original z_n were complex with magnitude $|z_n| = 1$ and uniformly randomly distributed. Total number of the data τ_i is $M = 128$, while $N = 64$. SNR is computed according to the following formula:

$$SNR(z) = 10log_{10}\left(\frac{\sum_i |z_i|^2}{\sum_i |\widehat{z}_i - z_i|^2}\right).$$

The experiment was rerun 20 times and the results were averaged. Results show that the LS Prony is stable and gives a pretty high SNR (30.26 dB for reconstructed z and 39.09 dB for the reconstructed data τ), though it is the lowest SNR among all methods. The Forward-Backward method has higher SNR than the LS Prony method because it uses additional information that all z_n lie on the unit circle. Among all methods, IQML gives the highest SNR (number of iterations for IQML was 5). The subspace-based method gives a significantly high SNR, a slightly outperforming the Total LS Prony method. In this experiment the Pencil-based method surprisingly gives the worst SNR. This experiment gives the flavor of different methods for solving the HR problem.

Chapter 4

Issues

In the process of acquiring real MRI data, there exist many different issues such as the limited speed of MRI scanner, limitations of acquisition protocols, and the existence of noise, which make our established mathematical model of JE problem deviate from what is really happening in practice. In the following sections we will discuss important issues that arise when implementing the proposed approach.

4.1 Condition on the Field Map Smoothness

The HR problem (2.10) solves for each of the columns of the image $f(\mathbf{n})$ and corresponding term $\phi_n = \omega(\mathbf{n})\delta_2 + \frac{2\pi}{N} n_2 \Delta_2$, but the order of ϕ_n (and hence, $f(\mathbf{n})$) in general cannot be preserved, since for any fixed n_1 reordering of $f(n)$ and ϕ_n does not change the data $s(\mathbf{m})$. To deal with this, we need the function $\omega(n_1, n_2)\delta_2 + \frac{2\pi}{N} n_2 \Delta_2$ to be monotonic, which requires the following constraint:

$$\omega[n_1, n_2]\delta_2 + \frac{2\pi}{N_2} n_2 \Delta_2 \quad < \quad \omega[n_1, n_2 + 1]\delta_2 + \frac{2\pi}{N_2}(n_2 + 1)\Delta_2, \tag{4.1}$$

which is equivalent to

$$\omega[n_1, n_2]\omega[n_1, n_2 + 1] < \quad \tfrac{2\pi\Delta_2}{N_2\delta_2}, \quad \forall n_1, n_2. \tag{4.2}$$

We call this condition the *monotonicity* condition.

4.2 Phase Unwrapping

Given recovered $\theta_{n_2} = -(\omega(n_2)\delta_2 + \frac{2\pi}{N} n_2 \Delta_2)$ for each fixed n_1, we need to recover field map ω_{n_2}. Here, we have phase warping problem, since actually $\theta_{n_2} = -(\omega(n_2)\delta_2 + \frac{2\pi}{N} n_2 \Delta_2) + 2\pi k_{n_2} n_2$, where k_{n_2} is any integer. The question is if we can estimate the unknown k_{n_2}. Defining $\Delta\theta = \theta_{n_2+1} - \theta_{n_2}$ we can easily get the following equation:

$$\Delta\theta = -\Delta\omega\delta_2 - \frac{2\pi\Delta_2}{N_2} + 2\pi\Delta k_{n_2}, \tag{4.3}$$

where $\Delta\omega = \omega(n_2 + 1) - \omega(n_2)$. Thus:

$$\Delta k_{n_2} = \frac{\Delta\theta + \frac{2\pi}{N_2}\Delta_2}{2\pi} + \frac{\Delta\omega\delta_2}{2\pi}. \tag{4.4}$$

Based on the fact that field map is smooth, we make an approximation $|\Delta\omega\delta_2| < \pi$. Then it follows that $\Delta k \approx \lceil(\Delta\theta + 2\pi\Delta_2/N_2)/(2\pi)\rceil$. Assuming $k_0 = 0$, we iteratively find the values $k_{i+1} = k_i + \Delta k$. Having these values of k_{n_2} we can recover the field map.

4.3 Noise Model

In the case of nonzero field map, the following question arises: what effect does noise in MRI data cause to the performance of the proposed algorithm? To answer this question, we first establish the noise model:

- *Noise in the data*: Each data sample $s[\mathbf{m}]$ at some position $\mathbf{m}$ is corrupted by additive uncorrelated Gaussian noise $\eta_s[\mathbf{m}]$ with zero mean and σ^2 variance.
- *Noise* $\eta_{\widetilde{s}}$: After taking an inverse DFT along each row of the data $s[\mathbf{m}]$ to get data samples $\widetilde{s}[n_1, m_2]$, the noise of these samples will have zero mean and σ^2/N_1 variance

[6]. Thus, corresponding noise $\widetilde{\eta}_s$ affected on *each column* $\widetilde{s}[m_2]$ has the following model:

$$\begin{aligned} \widehat{\widetilde{s}}[m_2] &= \widetilde{s}[m_2] + \eta_{\widetilde{s}}[m_2], \text{ for each fixed } n_1, \\ E[\eta_{\widetilde{s}}] &= 0, \\ E[\eta_{\widetilde{s}}\eta_{\widetilde{s}}^*] &= \frac{\sigma^2}{N_1} I. \end{aligned} \tag{4.5}$$

- *Noise in the recovered image*:

$$\widehat{f}[\mathbf{n}] = f[\mathbf{n}] + \eta_f[\mathbf{n}].$$

- *Noise in the recovered field map*:

$$\widehat{\omega}[\mathbf{n}] = \omega[\mathbf{n}] + \eta_\omega[\mathbf{n}].$$

By taking image and field map to be zero-constant, we can easily get the following relation between noises $\eta_{\widetilde{s}}$, η_f and η_ω exist:

$$\eta_{\widehat{s}} = Z\{e^{i\eta_\omega}\}\eta_f, \tag{4.6}$$

where $Z\{e^{i\eta_\omega}\}$ is a matrix Z in Eq. (3.7) with elements $z = e^{i\eta_\omega}$.

4.4 Effect of Noise on Performance of the Proposed Method

Recall the main Equation (2.9) of the proposed approach. For each fixed n_1, we call terms $-(\omega[\mathbf{n}]\delta_2 + \frac{2\pi}{N_2}n_2)$ with $n_2 = 0, ..., N_2 - 1$ the *harmonics*. Without a field map, these terms

become $-\frac{2\pi}{N_2}n_2$ terms which, when plotted, will give a straight line. A field map will make this line deviate and the proposed method requires that this deviated line satisfy the monotonicity condition. Noise in the field map η_ω can push some harmonic at position (n_1, n_2) too close to its neighbor harmonic at $(n_1, n_2 - 1)$ or $(n_1, n_2 - 1)$. Recall that in order to recover the image, all HR methods require inverting matrix Z in Eq. (3.7). Two closely spaced harmonics cause this matrix to be rank deficient, and thus, incorrect large pixel intensity will appear at the corresponding location in the recovered image.

To quantitatively estimate the effect of harmonic separations on the resulting reconstruction, we compute the *Crameér*-Rao bound (CRB)[1] of the estimated $\theta = -(\omega[\mathbf{n}]\delta_2 + \frac{2\pi}{N_2}n_2)$ and see how this bound changes when the harmonic separation is altered. In our case, we are interested in CRB of estimated harmonics $\theta = -(\omega(\mathbf{n})\delta_2 + \frac{2\pi}{N_2}n_2)$ column by column. This CRB has already been derived in [12], and other results on CRB were given in [14], [13]:

$$CRB_\theta = \frac{\sigma^2}{2} Re\{a * D * [I - Z(Z^*Z)^{-1}Z^*]Da\}, \tag{4.7}$$

where a is an image column, Z is a matrix defined in (3.7) and $D = \frac{dZ}{d\omega_i}$.

Applying monotonicity condition described in Eq. (4.2), we require the following constraint:

$$\eta_\omega[n_1, n_2] < \omega[n_1, n_2 + 1] - \omega[n_1, n_2] + \frac{2\pi}{N_2} + \alpha, \tag{4.8}$$

where α is a given fixed harmonic separation.

4.5 Real Data Acquisition: Limitations

Besides noise impact on the performance of the reconstruction, there exist other issues from a hardware aspect, especially during real data acquisition. We will consider these issues

[1]Cramer-Rao bound (CRB) gives a lower bound on the variance of the error between estimated $\widehat{\theta}$ and exact parameters θ of the model, and it is found through inverting the *Fisher information matrix*, which form can be found in [12]-[13].

below:

1. In reality, when scanning a line in k-space to acquire data samples, a MRI scanner cannot acquire data uniformly due to hardware limitations. Instead, at the right and left sides of the line data will be collected quicker, causing MRI data to be denser at these sides. [2] Such a Nonuniform data acquisition is illustrated in Fig. 4.1.

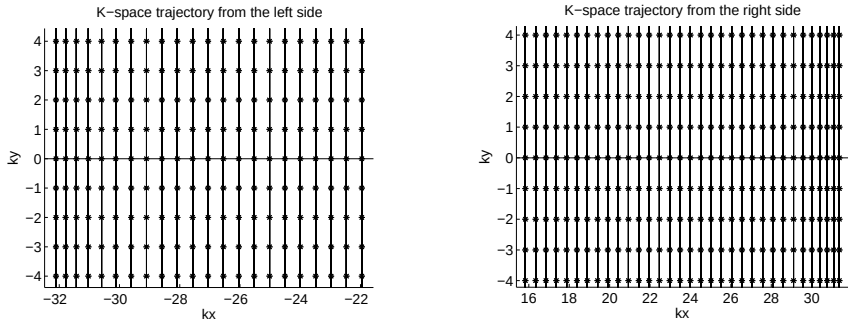

(a) (b)

Figure 4.1: Nonuniform acquisition. (a) Data samples in k-space from the left side. (b) Data samples in k-space from the right side.

   To get uniform data samples from Nonuniform data samples collected along EPI trajectory, gridding to a uniform grid procedure is used [15].

2. Another issue with real data acquisition arises from the fact that image magnitude depends also on parameters of MRI scanner. Thus, we can get different scaling of the acquired MRI data if we change these parameters. This is one reason why contrast is more important in MRI. In the case where ground true image and field map are known, we can simulate MRI data and find the ratio between the maximum range of simulated data to the maximum range of real data. Having this ratio, we can easily adjust acquired data to get closely to the correct scale.

3. Consider an example of acquiring 64×64 MRI data to recover an object and field map of the size 32. Using standard EPI acquisition sequence to traverse along EPI trajectory

[2] This means that δ_1 and δ_2 are no longer constants.

64×64 symmetric k-space region centered at the origin, the corresponding FOV in image domain will also be a symmetric 64×64 square region from $n_1 = -32, ..., 31$ and $n_2 = -32, ..., 31$. We call the produced data as $s_1[\mathbf{m}]$. However, since HR requires number of data samples to be at least two times of N_2, our model needs FOV of the size 32×64 with $n_1 = -31, ..., 32$ and $n_2 = -16, ..., 15$. Denote data samples in this case $s_2[\mathbf{m}]$. We find out that if the following condition is satisfied for both image and field map:

$$\begin{aligned} f_{2T}[n_1, 2n_2] &= f_{2T}[n_1, 2n_2 + 1] \\ \omega_{2T}[n_1, 2n_2] &= \omega_{2T}[n_1, 2n_2 + 1], \end{aligned} \tag{4.9}$$

the following relation between $s_1[\mathbf{m}]$ and $s_2[\mathbf{m}]$ holds:

$$s_2[\mathbf{m}] = \frac{s_1[\mathbf{m}]}{1 + e^{-i\frac{2\pi}{N} m_2 \Delta_2}}. \tag{4.10}$$

When condition (4.10) does not hold and gives a poor reconstruction, we use another acquisition protocol so that it produces the data $s_2[\mathbf{m}]$ directly. We call this acquisition scheme the *interleaved* scheme, and it is illustrated in the following figure. Consider the 96×64 symmetric k-space region. We acquire data samples along an EPI trajectory inside the first 64×64 region, then we jump back by a certain amount so that we can scan the last 64×64 region. The intersection of these two 64×64 regions give us the data $s_2[\mathbf{m}]$.

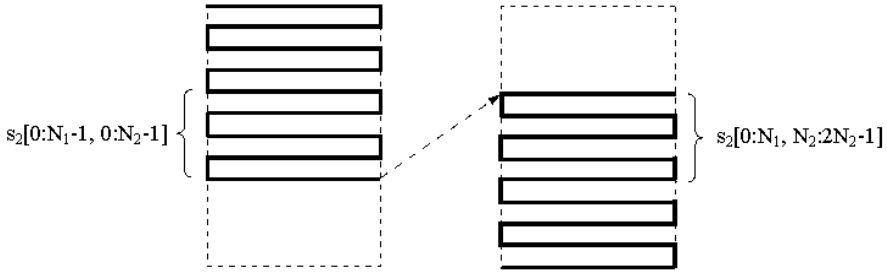

Figure 4.2: Interleaved acquisition.

Chapter 5

EXPERIMENTAL RESULTS

5.1 Simulated Data

We are interested in seeing how the proposed approach works on simulated data. In these experiments, a real MRI image and field map were acquired in accordance with the Internal Review Board (IRB) of Illinois. The MRI data is produced according to the following parameters: $\Delta_1 = \Delta_2 = 1$, $\delta_1 = 5\ \mu s$, $\delta_2 = 400\ \mu s$. We are interested in the SNR of the reconstructed image in two cases: with and without compensating for the field map. We also consider field maps satisfying and not satisfying the monotonicity condition (4.2). In the experiments shown below, the HR part was implemented using forward-backward method [9].

In the first case, field maps in the range from 15 Hz to 60 Hz were considered. In Fig. (5.1) one of these experiments is shown: the original field map has a maximum value of about 31.87 Hz. The results show that our approach recovers the original image and field map much better (SNR = 60.16 dB for the image and SNR = 47.79 db for the field map) compared to the case where field map is not considered (SNR = 4.41 dB).

In the second case, the original field map is more severe. It has a maximum value of 95.36 Hz (Fig. 5.2). In this case, due to the violation of the monotonic condition, at *a few* locations HR cannot recover the correct order of ϕ_n, thus, causing pixel shifts and gaps in the reconstructed images. We further postprocess the images to keep track of the gaps and then shift back all pixels. The resulting SNR for the recovered image is 18.94 dB, while the reconstruction without the field map gives SNR = 2.39 dB. The recovered field map has poor

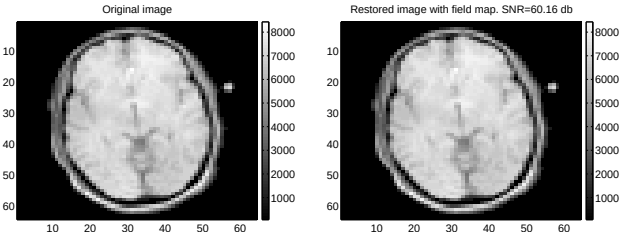

(a) Original 64×64 image. (b) Recovered image SNR = 6.16 dB (c) Original field map, max. value: 31.87 Hz. (d) Recovered field map SNR = 47.70 dB

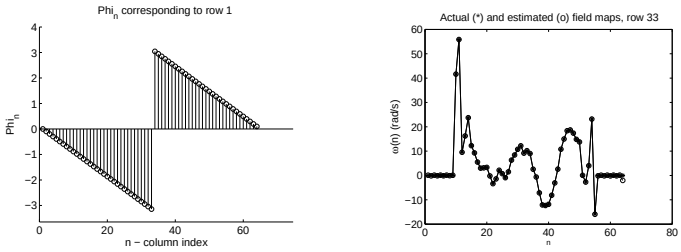

(e) Monotonicity condition is held, column 1. (f) Actual (*) and estimated field maps, column 33. (g) Recovered image without field map, SNR = 4.41 dB.

Figure 5.1: Experiment with moderate field map.

SNR = -0.09 db; however, its original shape and some details are highly preserved. We can see that reconstructed images without field map are greatly distorted in the region of field inhomogeneity (Fig. 5.2(d)). Note also that with the increasing range of field inhomogeneity, the approximation $\omega(\mathbf{n})\delta_1 \approx 0$ is less preserved.

Another advantage of this method is running time. By making the approximation $w(\mathbf{n})\delta_1 \simeq 0$, we map the original 2-D problem into a sequence of 1-D HR problems, which reduces execution time dramatically compared to the CG method [3]. The program was run on an Intel Pentium 1.6 GHz CPU, 1.25 GB RAM computer. For a 64×64 image, the running time is about 13 s. With a 90×90 image, the running time is about 43 s.

5.2 Real Data

Real MRI data are produced by scanning a real phantom using Siemens MRI machine at Biomedical Imaging Center in accordance with the Internal Review Board (IRB) of Illinois. The phantom is a plastic bottle filled with distilled water. Inside was a small ball filled with

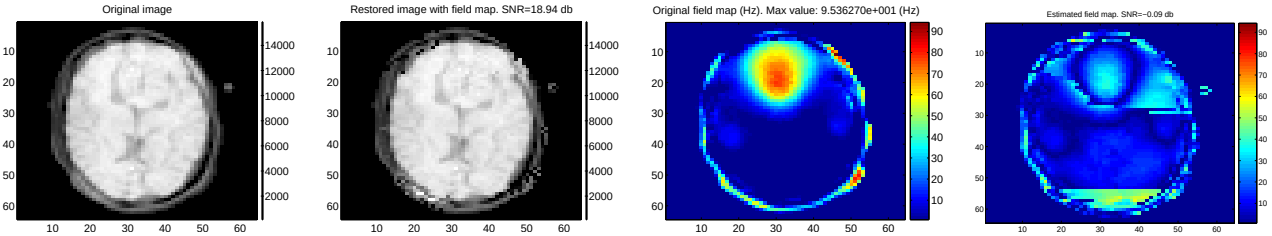

(a) Original 64×64 image. (b) Recovered image SNR = 18.94 dB. (c) Original field map, max. value: 95.36 Hz. (d) Recovered field map SNR = -0.09 dB.

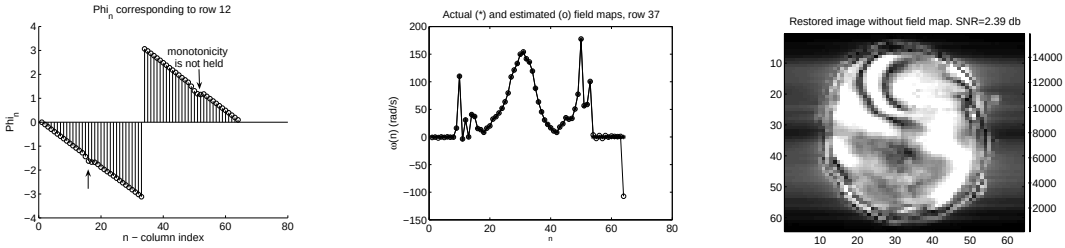

(e) Monotonicity condition is not held, column 12. (f) Actual (*) and estimated field maps, column 37. (g) Recovered image without field map, SNR = 2.39 dB.

Figure 5.2: Experiment with severe field map.

air, to cause susceptibility distortions. Figure 5.3 shows a 2-D slice of object and field map of size 32×64 as a ground truth for reconstruction comparisons. The field map has effect only in the region close to the boundary of the object, and its maximum range is 61.77 Hz.

(a) Original object. (a) Original field map.

Figure 5.3: Ground truth.

Figure 5.4 shows real acquired data versus simulated data in the (n_1, m_2) space which we will call as *half k-space domain*. We see that both simulated and real data have two peaks, which agree with our model. [1] However, these two data sets are quite different from each other in the shape of the peaks and in the scaling. The reason for the difference in the

[1]The part of the data having $m_2 = 0, ..., 31$ gives one peak at the center and the left part of the data corresponding to $m_2 = 32, ..., 63$ gives another aliased peak.

scaling comes from the fact that image magnitude depends also on the input parameters of MRI scanner such as T_1, T_2 relaxation parameters.[2]

(a) Simulated data $[64 \times 64]$ in half k-space domain.

(b) Real data $[32 \times 64]$ in half k-space domain before scaling.

Figure 5.4: Comparison between simulated and real data.

Reconstruction using real data gives the image shown in Fig. 5.2(a). As we can see,[3] there are some wrong large-valued pixels and this result is worse than the reconstruction using simulated data (Fig. 5.5(f)). Consider one particular wrong pixel with a very large intensity, at the row 9 and column 30. Tracking back on the angle of $z = e^{-(\omega(\mathbf{n})\delta_2 + \frac{2\pi}{N_2} n_2)}$ computed from HR stage, from Fig. 5.2(b), we confirm that a harmonic at $n_2 = 9$ is really close to its preceding harmonic at $n_2 = 8$. The separation between these two harmonics is 0.01.

Using Eq. (4.7) we compute CRB_θ at different harmonic separations for this data set. Noise variance $\sigma^2 = 1$ and separation amount g was varying from 0 to 0.1. Since the algorithm operates column by column, for each image column we have different CRB plot. The resulting plot for the column 7 is shown in Fig. 5.5(e). This plot is similar to the plot shown in [14]. Specifically, as the separation gets smaller, CRB_θ is larger. When $g = 0$, CRB_θ blows up. In the worst case $CRB_\theta \approx 6.4$ for $g = 0.01$.

Using available information from the plots of harmonics (angle of z), we predict which pixel will be incorrectly recovered and we replace that pixel value by an interpolated intensity of neighbor pixels. The resulting image has an improved SNR and it is shown in Fig. 5.2(c).

[2]That is why in MRI contrast is more important than image intensity range.

[3]Note that since the ground true data have different scaling than acquired data, SNR in real reconstruction is low.

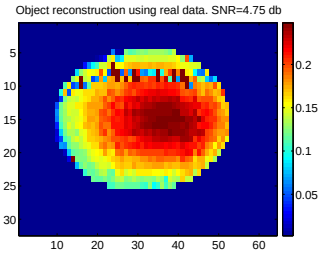

(a) HR reconstruction from real data.

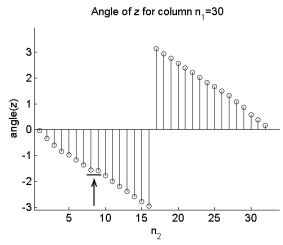

(b) Angle of z at column 30.

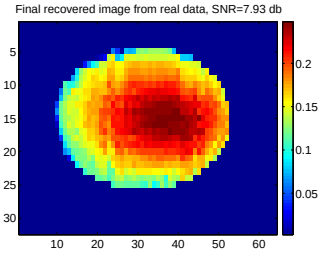

(c) HR reconstruction from real data after predicting wrong pixels.

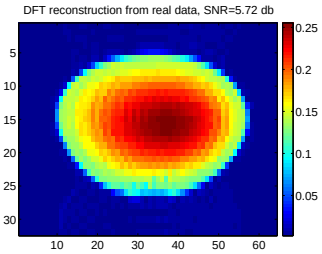

(d) DFT reconstruction.

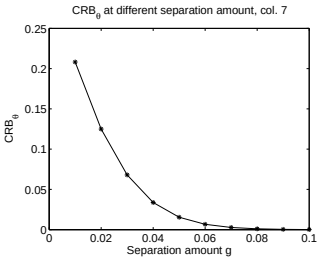

(e) CRB_θ plot.

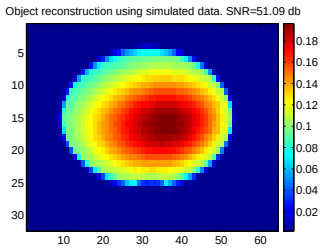

(f) HR reconstruction from the simulated data.

Figure 5.5: HR and DFT reconstruction from the real and simulated data. CRB_θ plot.

Reconstruction from simulated data obviously has the best SNR (Fig. 5.5(f)) and a direct DFT reconstruction gives a distorted image (Fig. 5.2(d)).

Chapter 6

CONCLUSIONS

In this work, we propose a new method for the MRI joint estimation (JE) problem by making a practical approximation that gives us two advantages. First, the nonlinear JE problem is transformed to a linear problem. Second, this approximation helps us to convert from a 2-D JE problem into a 1-D HR problem. To make a bridge between the JE and HR problems, we need a condition on the smoothness along vertical direction of the original field map or its variation range. With small and medium variation of the field map, our approach recovers the image from simulated data much better in comparison to the method without the field map. In the case of the severe field map, we can still reconstruct all details and shape of the image, with slight pixel shifts. The resulting estimated field map can also be used as an initial guess for other Joint Estimation methods [3]. During real data acquisition there exist issues which affect the performance of the algorithm. Specifically, noise in the collected data makes original harmonics to be closely spaced with each others. We use this fact to avoid incorrectly recovered pixels. The main advantage of this approach is that it does not require a prior knowledge of the field map and has low complexity. The resulting estimated field map can also be used as an initial guess for other JE methods [3].

References

[1] P. Jezzard and R. S. Balaban, "Correction for geometric distortion in echo planar images from B_0 field variations," *Magnetic Resonance in Medicine*, vol. 33, p. 65, 1995.

[2] D. B. Twieg, "Parsing local signal evolution directly from a single-shot MRI signal: A new approach for fMRI," *Magnetic Resonance in Medicine*, vol. 50, p. 1043, 2003.

[3] B. P. Sutton, D. C. Noll, and J. A. Fessler, "Dynamic field map estimation using a spiral-in/spiral-out acquisition," *Magnetic Resonance in Medicine*, vol. 51, p. 1194, 2004.

[4] H. M. Nguyen, R. Morrison, B. Jr., and M. N. Do, "Joint estimation in MRI using harmonic retrieval methods," *in IEEE International Symposium on Biomedical Imaging*, p. 53, 2006.

[5] E. Schneider and G. Glover, "Rapid in vivo proton shimming," *Magnetic Resonance in Medicine*, vol. 18, p. 335, 1991.

[6] Z.-P. Liang and P. C. Lauterbur, *Principles of Magnetic Resonance Imaging: A Signal Processing Perspective*, 1st ed. IEEE Press Series on Biomedical Engineering, 2000.

[7] M. Vetterli and J. Kovacevic, *Wavelets and Subband Coding*. Prentice Hall, 1995.

[8] M. Vetterli, J. Kovacevic, and V. K. Goyal, *The World of Fourier and Wavelets: Theory, Algorithms and Applications*. Lecture notes from ECE 598-MD class, 2005.

[9] M. Elad, P. Milanfar, and G. H. Golub, "Shape from moments - an estimation theory perspective," *IEEE Transactions on Signal Processing*, vol. 52, p. 1814, July 2004.

[10] Y. Bresler, S. Basu, and C. Couvreur, *Hilbert Spaces and Least Squares Methods for Signal Processing*. Lecture notes from ECE 534 class, Feb, 2001.

[11] I. Maravic and M. Vetterli, "Sampling and reconstruction of signals with finite rate of innovation in the presence of noise," *IEEE Transactions on Signal Processing*, vol. 53, Aug 2005.

[12] P. Stoica and A. Nehorai, "MUSIC, maximum likelihood, and Cramer-Rao bound," *IEEE Transactions on Acoustics, Speech, and Signal Processing*, vol. 37, p. 720, May 1989.

[13] J. C. Ye, Y. Bresler, and P. Moulin, "Cramer-Rao bounds for parametric shape estimation in inverse problems," *IEEE Transactions on Image Processing*, vol. 12, p. 71, Jan 2003.

[14] S. F. Yau and Y. Bresler, "Worst case Cramer-Rao bounds for parametric estimation of superimposed signals with applications," *IEEE Transactions on Signal Processing*, vol. 40, p. 2973, Dec 1992.

[15] J. I. Jackson, C. H. Meyer, D. G. Nishimura, and A. Macovski, "Selection of a convolution function for Fourier inversion using gridding," *IEEE Transactions on Medical Imaging*, vol. 10, p. 473, Sep 1991.